

De novo simulation of charge transport through organic single-carrier devices

Simon Kaiser,[†] Naresh B. Kotadiya,[‡] Roland Rohloff,[‡] Artem Fediai,[†] Franz Symalla,[¶] Tobias Neumann,[¶] Gert-Jan A.H. Wetzelaer,[‡] Paul W.M. Blom,[‡] and Wolfgang Wenzel^{*,†}

[†]*Institute of Nanotechnology, Karlsruhe Institute of Technology (KIT),
Hermann-von-Helmholtz-Platz 1, 76344 Eggenstein-Leopoldshafen, Germany*

[‡]*Max Planck Institute for Polymer Research, Ackermannweg 10, 55128 Mainz, Germany*

[¶]*Nanomatch GmbH, Griesbachstr. 5, 76185 Karlsruhe, Germany*

E-mail: wolfgang.wenzel@kit.edu

Abstract

In amorphous organic semiconductor devices, electrons and holes are transported through layers of small organic molecules or polymers. The overall performance of the device depends both on the materials and the device configuration. Measuring a single device configuration requires a large effort of synthesizing the molecules and fabricating the device, rendering the search for promising materials in the vast molecular space both non-trivial and time-consuming. This effort could be greatly reduced by computing the device characteristics from first principles. Here we compute transport characteristics of unipolar single-layer devices of prototypical hole and electron transport materials respectively *N,N'*-Di(1-naphthyl)-*N,N'*-diphenyl-(1,1'-biphenyl)-4,4'-diamine (α -NPD) and 2,2',2''-(1,3,5-Benzinetriyl)-tris(1-phenyl-1-H-benzimidazole) (TPBi) using a first principles multiscale approach that requires only the molecular constituents and the device geometry. This approach of generating a digital twin of the entire device can be extended to multi-layer stacks and enables computer design of materials and devices to facilitate systematic improvement of organic light-emitting diode (OLED) devices.

1 Introduction

Modern organic light-emitting diodes (OLEDs) are composed of multiple thin layers of small organic molecules, each of which must be carefully optimized to play its integral role in the device performance. Holes and electrons are injected into hole- and electron-transporting layers (HTL and ETL) directly from the electrode or indirectly via a doped injection layer and traverse the system in opposite directions to recombine in one or more emissive layers. For efficient device operation, it is crucial that charges are injected and transported efficiently in both the HTL and ETL, providing both types of charge carriers to the emissive layer

(EML) at a high and balanced rate.

The injection into the HTL and ETL is governed by the ionization potential (IP) and electron affinity (EA), respectively, of the molecules in the thin films with respect to the electrode work function, as well as the disorder of polaron energy levels (σ)¹. The transport properties are governed by the charge-carrier mobility, which mainly depends on σ , the electronic couplings and the presence of deep traps^{2,3}. In the case of efficient charge injection, i. e. with ohmic contacts, the current through a device will be space-charge limited, the magnitude of which depends on the temperature-, field- and density-dependency of the mobility⁴. While the IP of the ETL and the EA of the HTL are not

relevant for charge transport to the EML, they are important for confinement of charges and excitons inside the EML.

Traditionally, experimental techniques are used to develop materials with appropriate IP and EA for optimizing injection and energy-level matching with the EML. While gas-phase IP and EA of the molecules can be calculated straightforwardly and provide a first hint at their suitability, they deviate from the bulk values because of polarization effects which ultimately require experimental measurements to obtain reliable values. Among current methods for measuring IP and EA of a material are ultraviolet phosphorescent spectroscopy (UPS) and low-energy inverse photoemission spectroscopy (LEIPS). These methods account for the influence of the polarizable medium, but are limited to typical accuracies of about 200 meV⁵ and 100 meV⁶ for EA and IP, respectively. Deviations of this magnitude remain significant, since the injected current depends exponentially on the injection barrier⁷.

Experimentally, the charge-carrier mobility of an organic film can be extracted from the space-charge-limited current (SCLC) through a thin layer with ohmic contacts⁸ or the time-of-flight (TOF) of induced charge carriers in a micrometer-thick sample⁹. In SCLC measurements injecting contacts have to be carefully optimized to eliminate injection barriers, while TOF measurements require trap-free and non-dispersive charge transport for a reliable evaluation of the transient mobility.

Each step in the device fabrication – from synthesizing the molecules, depositing pristine layers, fabricating devices to measuring relevant parameters – is both challenging and time-consuming. Even with all the parameters measured, the exact behaviour of the OLED is difficult to predict, requiring fabrication of multiple samples with different configurations to develop an efficient OLED. *Ab initio* multiscale workflows can help screen molecules and device configurations for the desired properties^{3,10,11}.

In prior work, we employed such a multiscale workflow to investigate charge transport in guest-host systems¹², performance of model OLED stacks^{13,14}, doped injection layers¹⁵ and photoluminescent quenching¹⁶. In this work we demon-

strate *de novo* simulations of two unipolar single-layer devices featuring ohmic charge injecting electrodes. To this end, we characterize material properties of α -NPD and TPBi, two molecules commonly used as hole- and electron-transport material in OLEDs, respectively. Based on these properties, we simulate charge transport in devices and calculate experimentally validated I - V characteristics. The charge transport model fully accounts for the amorphous structure of the materials and the many-body interaction of charge carriers – in contrast to previous works^{10,17} – which can lead to significant errors in the regime of ohmic injection^{18,19}. With only the molecular structure and electrode work functions as input, the final current density–voltage characteristics show a very good agreement with experiment. Development of such a multiscale workflow paves the way for the in-depth study and computational design of multi-layer organic semiconductor (OSC) devices like OLEDs and organic solar cells (OPVs).

2 Experiment

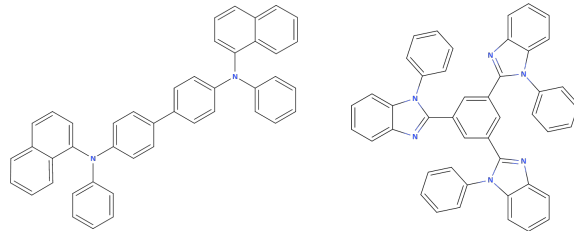


Figure 1: Single carrier devices investigated here are composed of α -NPD (left) and TPBi (right).

Hole-only devices were fabricated by sandwiching a thermally evaporated layer of N,N' -Di-(1-naphthyl)- N,N' -diphenyl-(1,1'-biphenyl)-4,4'-diamine (α -NPD) (100 nm) between a hole-extracting bottom electrode consisting of poly-(2,3-dihydro-thieno-1,4-dioxin):poly(styrenesulfonate) (PEDOT:PSS)-covered indium-tin oxide and an ohmic hole-injecting top electrode consisting of a 5 nm 4,4',4''-tris(N -carbazolyl)-triphenylamine (TCTA) interlayer, a 10 nm MoO₃ layer, and a 100 nm Al layer consecutively evaporated on top of the α -NPD layer. The TCTA tunneling interlayer prevents the formation of a hole-injection barrier¹⁷, providing ohmic hole injection

from the top electrode. Electron-only devices consist of a thermally evaporated layer of 2,2',2''-(1,3,5-Benzinetriyl)-tris(1-phenyl-1-H-benzimidazole) (TPBi) (115 nm) sandwiched between an electron extracting Al (30 nm) bottom electrode and an electron-injecting Ba(5 nm)/Al(100 nm) top electrode. The current density–voltage characteristics were measured under N_2 atmosphere with a computer-controlled Keithley 2400 source meter at various temperatures.

3 Multiscale approach

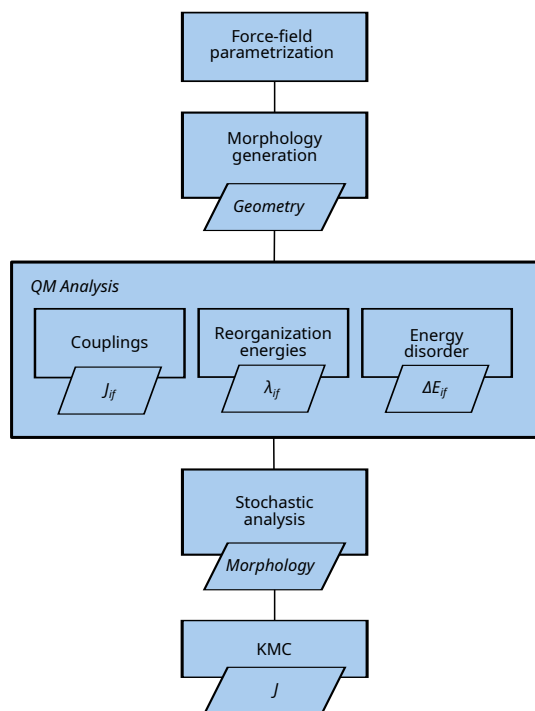


Figure 2: Multiscale workflow used to bridge length- and timescales required for the device simulations. Classical force-fields are parametrized with the molecular structure using DFT²⁰. DEPOSIT²⁰ uses these force-fields to deposit an amorphous morphology. DFT calculations with the QuantumPatch²¹ method provide parameters for the Marcus Rate. A stochastic expansion method^{12,22} generates an amorphous device structure from the deposited morphology and data from the QM Analysis. Charge transport in the device is simulated with a kMC device model¹².

To calculate the current density–voltage characteristics for the different devices, we use the

multiscale workflow depicted in fig. 2. The molecular structure is first optimized with density-functional theory (DFT)²³ and used to parametrize a molecule-specific force-field²⁰, which is subsequently used in a Monte-Carlo deposition scheme²⁰ mimicking physical vapor deposition to generate a morphology. IP, EA, reorganization energy and electronic couplings of the molecules in their unique environment within the morphology are analyzed using DFT in a self-consistent electrostatic embedding scheme²¹. A stochastic expansion method^{12,22} creates device-scale amorphous structures from the deposited morphologies and parameters from the DFT calculations. Finally, polaron dynamics in the amorphous structure are modelled with a kinetic Monte-Carlo (kMC) method¹². All DFT calculations are performed using the DFT package Turbomole²⁴ with the B3LYP²⁵ functional and def2-SVP²⁶ basis set unless noted otherwise.

3.1 Material morphology

To obtain representative atomistic models of the amorphous thin-film for each material, 1000 molecules are deposited using the Monte Carlo (MC) based DEPOSIT²⁰ protocol mimicking the physical vapour deposition process. The molecules are sequentially added to a simulation box of $80 \text{ \AA} \times 80 \text{ \AA} \times 300 \text{ \AA}$ with periodic boundary conditions in x- and y-direction and positions, orientations and dihedral angles are sampled using a simulated annealing (SA) algorithm. Molecule-specific intramolecular force-fields are derived by computing DFT energies of single molecules in vacuum with step-wise rotated dihedral angles. Bond distances and angles are kept fixed during deposition. Intermolecular interactions are modeled using Coulomb potentials based on the computed ESP charges and Lennard-Jones potentials derived using the DEPOSIT force-field. In each SA cycle, the molecule samples the morphology surface starting from an artificially high temperature (4000 K) to room temperature (300 K) in 150000 MC steps, providing sufficient sampling for the organic molecules studied here²⁷. To improve sampling, 32 SA cycles are run in parallel with the final candidate selected based on the Metropolis-criterion²⁸.

3.2 Electronic properties

In these morphologies IP and EA, reorganization energies (λ_i), distribution of HOMO and LUMO energies as well as electronic couplings (J_{if}) of a subset of molecules in their unique environment are calculated using the QuantumPatch²¹ method. The QuantumPatch method self-consistently equilibrates the charge density of molecules in the morphology. IP and EA are calculated as the total energy difference of single molecules in the charged and uncharged state within the morphology. The reorganization energies λ_i are calculated based on Nelsen’s four point procedure²⁹. The geometry of each molecule is optimized in the charged and uncharged state with the constraints imposed by the environment modeled with effective core potentials at the positions of surrounding atoms. The conformational response of the environment is neglected. The disorder σ is calculated from the distribution of $\Delta E_{\text{HOMO/LUMO}}$ of neighbouring molecules. Electronic coupling elements are calculated from the hopping-matrix elements of dimers for charged–uncharged-pairs following the Löwdin orthogonalization procedure^{30,31} using the BP86^{32,33} functional³⁴. For the pair selection, we apply an atom–atom-distance cutoff of 7 Å, a value much larger than the typical π – π -stacking distance where the electronic coupling is already insignificantly small (see fig. S1). Each calculation is done in the converged electrostatic environment of the molecules.

3.3 Structure expansion

The device simulations require amorphous structures much larger than the deposited morphology³⁵. Structures in device scale are generated from the deposited morphology using an extension of the dominance competition model of Baumeier *et al.*²² presented in prior work¹². The IP and EA of each site in the resulting amorphous structure is drawn from the gaussian distribution with width σ and center at the microscopic IPs and EAs. Electronic coupling elements J_{if} for each site i and connected sites f with a pair distance of r_{if} are drawn from the microscopic distribution of electronic couplings J' within a small interval dr around r_{if} . Connectivity of a given pair is deter-

mined by the probability of a center of mass distance r_{if} relating to an atom–atom-distance below the cutoff in the electronic structure calculation. Reorganisation energies are taken to be constant.

3.4 Charge transport

Charge transport through the device is simulated using the kMC model implemented in the lightforge (LF) package¹². Charge transport is modelled as hopping process between a site i and one of the connected sites f with the Marcus-rate³⁶

$$k_{if} = \frac{2\pi}{\hbar} |J_{if}|^2 \frac{1}{\sqrt{4\pi\lambda k_B T}} \exp\left(-\frac{(\lambda + \Delta E_{if})^2}{4\lambda k_B T}\right), \quad (1)$$

where J_{if} is the electronic coupling, λ the reorganization energy, T the temperature and ΔE_{if} the energy difference between the charge carrier occupying site i and site f including energetic disorder, applied field and dynamic electrostatic potential from all charges in the system. The electronic coupling J_{if} contains both the direct electronic coupling of sites i and f and the superexchange coupling via any of the N neighbouring sites j as bridge molecules using first-order perturbation theory

$$J_{if} \simeq J_{if,0} + \sum_{n=1}^N \frac{J_{in,0} J_{nf,0}}{E_{\text{virt}} - E_T}, \quad (2)$$

where $J_{if,0}$ is the direct electronic coupling of sites i and f , E_{virt} is the energy of the system in its virtual state with the charge on the bridge molecule j and E_T the transition state energy¹².

The dynamic electrostatic potential is reevaluated after each charge movement by calculating the electrostatic Ewald Sum³⁷ including all charges in the system and an infinite series of image charges due to the metallic boundary conditions at the electrodes.

To account for the ability of the electrodes to dissipate continuous amounts of energies, charge injection and extraction is modelled with the Miller–

Abrahams³⁸ rate

$$k_{ij} = \frac{\pi}{2k_B T} |J_{ij}|^2 \begin{cases} \exp\left(\frac{-\Delta E_{ij}}{4k_B T}\right), & \text{for } \Delta E_{ij} > 0 \\ 1, & \text{otherwise} \end{cases} \quad (3)$$

with the injection barrier

$$\Delta E_{ij} = W_j - E_i - \phi_{\text{screen}} - \phi_{\text{dyn}} - q\vec{F} \cdot \vec{r}_{ij} \quad (4)$$

between the electrode j and a site i at distance \vec{r}_{ij} including the difference in work function W_j and site energy E_i , electronic screening ϕ_{screen} due to the electrode, dynamic electrostatic potential ϕ_{dyn} from other charges in the system and the applied electric field \vec{F} . The barrier at the extracting contact is defined analogously. To account for stochasticity in morphology expansion and site-energy distribution, 10 different configurations are sampled per applied field. Convergence is reached when the current density is constant over two thirds of the simulation.

4 Results

We apply the presented multiscale workflow to calculate material properties for α -NPD and TPBi, two materials commonly employed in hole or electron transport layers of modern OLEDs, respectively. Subsequently, we simulate device characteristics of unipolar single-layer devices composed of these materials at different driving voltages and temperatures. Both the material properties (table 1) and device characteristics (fig. 4) are in good agreement with experimental data.

The nearest-neighbour-distributions of extended structures, depicted in fig. 3, closely match that of the deposited morphology with a slight trend to underestimate the distribution at small distances and overestimate the peaks of the distribution. These small deviations, however, have only little impact in the charge transport through the devices. Figure 4 shows the simulated current densities compared to experimental measurements. With decreasing voltage the probability for a charge carrier to overcome the attractive potential of its image charge decreases, leading to an increasing part of the simulation time being spent on charge injection, extraction and hops along the electrode–HTL

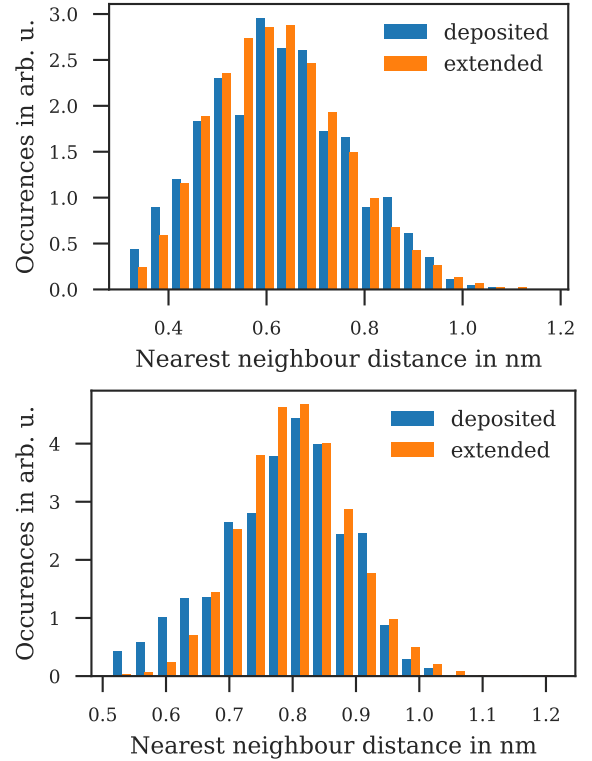


Figure 3: Nearest-neighbour distribution of the deposited morphology (blue) and expanded structure (orange) of α -NPD (top panel) and TPBi (bottom panel).

interface, requiring a trade-off between level of detail and simulation time. We therefore limit our simulations to current densities above 100 A m^{-2} for α -NPD and 10 A m^{-2} for TPBi. The simulated current densities agree well with the experimental current densities over a broad range of voltages and temperatures. Both devices feature ohmic contacts, even accounting for the differences in built-in voltages, however, the TPBi device shows lower current densities at comparable applied voltages than the α -NPD device, mainly caused by larger ΔE_{ij} in the exponent of eq. (1) due to the larger disorder in the TPBi device.

Charge carriers inject from the ohmic contacts, shifting the vacuum level until the edge of the transport level aligns with the electrode work function. The resulting space-charge effectively shields the interface region from the external electric field, leading to flat transport levels in the vicinity of the injecting electrode and in turn amplifying the external field far away from this electrode. Both effects are evident in the distribution of site energies, i. e. IP or EA with the external field ap-

Table 1: Microscopic input parameters for the charge transport simulations of the α -NPD and TPBi device calculated with the QuantumPatch method²¹. Namely ionization potential (IP), electron affinity (EA), disorder (σ), reorganization energy (λ) and average electronic couplings ($\langle J^2 r^2 \rangle$) along with references to literature values where available.

Molecule	IP/eV	EA/eV	σ /meV	λ /meV	$\langle J^2 r^2 \rangle$ /eV ² Å ²
α -NPD	5.48 ³⁹⁻⁴¹	1.93 ^{39,41}	96 ^{42,43}	216	1.57×10^{-3}
TPBi	6.79 ⁴⁴	2.07 ⁴⁴	162	237	2.33×10^{-3}

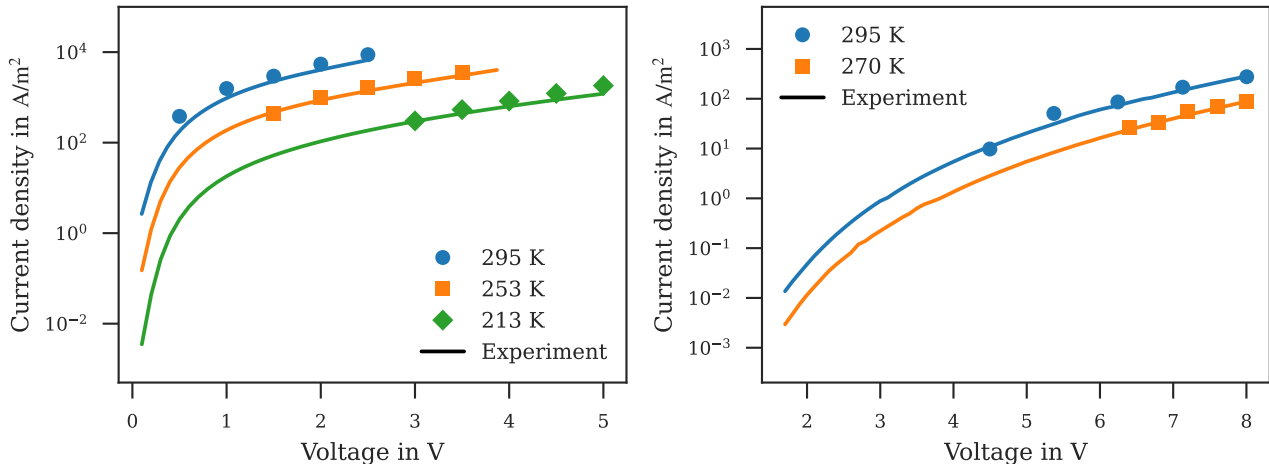


Figure 4: Simulated J - V characteristic of α -NPD (left) and TPBi (right) at different operating temperatures compared with experiment. Simulation errors are of the order of symbol size.

plied and the dynamic coulomb potential of the charges in the system, depicted in the top panel of fig. 5. The bottom panel of fig. 5 shows the charge densities in slices of 1 nm in transport direction averaged over the second half of the simulation. As can be seen, most charge carriers are situated in the space-charge region or, in the α -NPD device, next to the extracting electrode. The exact charge density at the electrodes depends on the injection barrier, leading to large charge-carrier densities at the ohmic injecting electrodes, slightly lower hole-density at the extracting electrode of the α -NPD device with a small initial barrier of 0.2 eV and a negligible electron-density at the extracting electrode of the TPBi device with a large initial barrier of 1.7 eV. Small features in the average charge densities far away from the electrodes are caused by shallow traps leading to longer occupation times. Due to the larger disorder, traps are more likely to occur in the TPBi device, resulting in stronger fluctuations of the average charge density in the bulk of this device than in the α -

NPD device. In the simulations, the probability of a charge carrier escaping the space-charge region is small, with the subsequent propagation through the bulk of the device being fast compared to the escape time. The exact ratio determines the current density J and depends on the applied voltage V and charge-carrier mobility in the device μ , recovering the Mott-Gurney equation⁴ $J \sim \mu V^2$ in the space-charge limited regime.

5 Conclusion

We presented a multiscale workflow to determine both material properties and the charge transport characteristics in single-carrier devices made from these materials without experimental input. In this approach we start from the generation of morphologies based on molecular mechanics calculations²⁰, which are then analyzed with electronic structure calculations using a quantum embedding method²¹. These data are then transferred via an extension scheme to kinetic Monte Carlo simu-

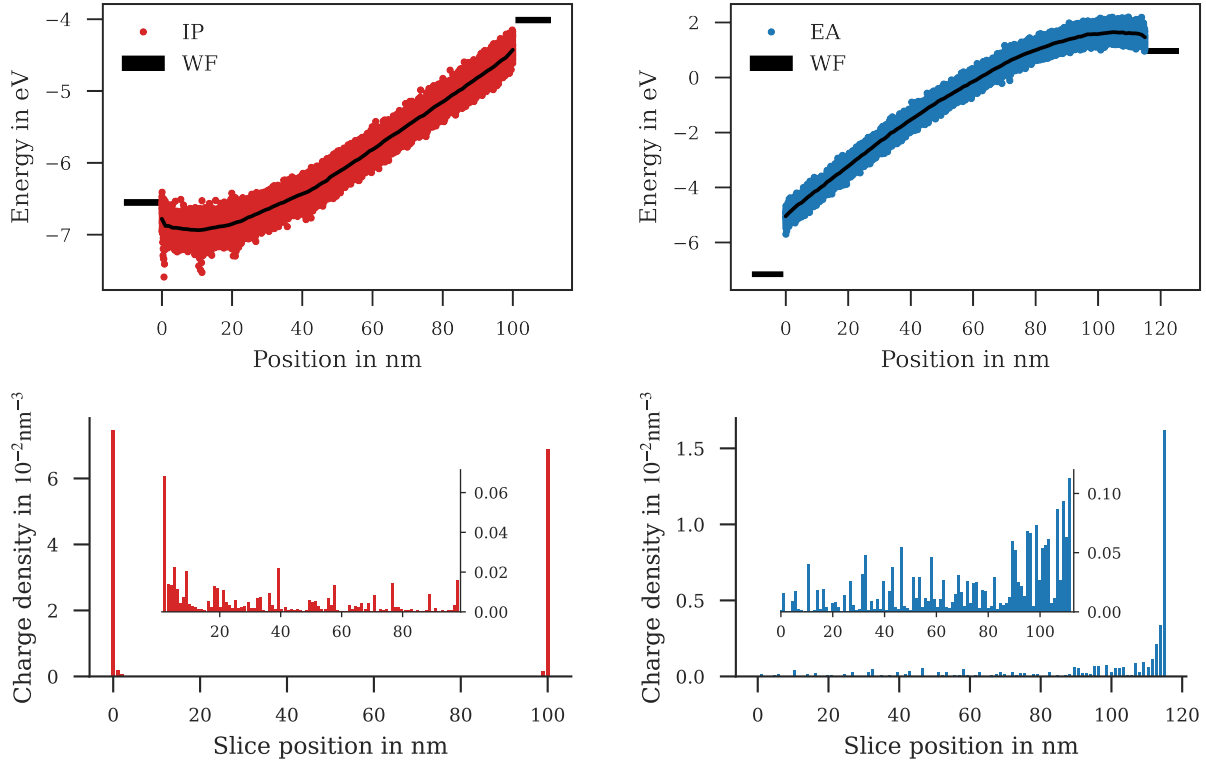


Figure 5: Insight into the α -NPD (left) and TPBi (right) devices with a Voltage of 2.5 V and 8 V applied respectively. Top panels: Energy diagram depicting each site energy including applied field and dynamic coulomb potential of all charges in the system averaged over 1000 kMC steps. Outliers are artifacts when sites are partially occupied during the short averaging window. Bottom panels: Charge density in slices of 1 nm in transport direction averaged over half of the simulation.

lations to compute the I - V characteristics. This approach shows good agreement to experimental data for single-carrier devices comprising α -NPD and TPBi, two prototypical materials in hole and electron transport materials, respectively. This demonstrates that a multiscale approach is now capable to characterize complex electronic devices *de novo* without experimental input. This multiscale workflow can be easily extended to model multi-layer devices enabling in-depth studies of multi-layer devices like OLEDs and OPVs^{13,14}. The bottleneck here is solely the computational cost of the kMC calculations, which are presently improved in other work.

Broadening the emission zones can reduce exciton quenching processes, which are among the prime reasons for OLED degradation³⁵. The width of the emission zone depends on the penetration depth of charge carriers into the emissive layer. An excess of electrons or holes leads to excess exciton formation close to the HTL- or ETL-EML interface respectively. Tuning the transport prop-

erties of both HTL and ETL to increase carrier-balance in the EML can thus increase both efficiency and lifetime of OLED devices³⁵. The developed workflow enables future studies to investigate transport properties in detail and thus aid in optimizing OLED devices.

Acknowledgement This project received funding from the European Union Horizon 2020 research and innovation programme under grant agreement no. 646176 (EXTMOS). S.K. received funding by the High-Performance Computing 2 program of the Baden-Württemberg Stiftung (Project MSME). W.W. acknowledges funding by the Deutsche Forschungsgemeinschaft (DFG) in the Research and Training Program “Tailored Scale Bridging Approaches to Computational Nanoscience” and under Germany’s Excellence Strategy — 2082/1 — 390761711 (3DMM2O).

Supporting Information Available

The Supporting Information, containing additional details on electronic property calculations and the sensitivity of computed current densities on parameter variations, is available free of charge at the publisher's website.

References

- (1) Ng, T. N.; Silveira, W. R.; Marohn, J. A. Dependence of Charge Injection on Temperature, Electric Field, and Energetic Disorder in an Organic Semiconductor. *Phys. Rev. Lett.* **2007**, *98*, 066101.
- (2) Bäessler, H. Charge Transport in Disordered Organic Photoconductors a Monte Carlo Simulation Study. *Phys. Status Solidi B* **1993**, *175*, 15–56.
- (3) Kordt, P.; van der Holst, J. J. M.; Helwi, M. A.; Kowalsky, W.; May, F.; Badinski, A.; Lennartz, C.; Andrienko, D. Modeling of Organic Light Emitting Diodes: From Molecular to Device Properties. *Adv. Funct. Mater.* **2015**, *25*, 1955–1971.
- (4) Mott, N. F.; Gurney, R. W. *Electronic Processes in Ionic Crystals*, 2nd ed.; The International Series of Monographs on Physics; Clarendon Pr.: Oxford, 1957.
- (5) Tadayyon, S. M.; Grandin, H. M.; Griffiths, K.; Coatsworth, L. L.; Norton, P. R.; Aziz, H.; Popovic, Z. D. Reliable and Reproducible Determination of Work Function and Ionization Potentials of Layers and Surfaces Relevant to Organic Light Emitting Diodes. *Org. Electron.* **2004**, *5*, 199–205.
- (6) Yoshida, H. Measuring the Electron Affinity of Organic Solids: An Indispensable New Tool for Organic Electronics. *Anal. Bioanal. Chem.* **2014**, *406*, 2231–2237.
- (7) van der Holst, J. J. M.; Uijtewaal, M. A.; Ramachandhran, B.; Coehoorn, R.; Bobbert, P. A.; de Wijs, G. A.; de Groot, R. A. Modeling and Analysis of the Three-Dimensional Current Density in Sandwich-Type Single-Carrier Devices of Disordered Organic Semiconductors. *Phys. Rev. B* **2009**, *79*, 085203.
- (8) Blom, P. W. M.; de Jong, M. J. M.; Vlegaar, J. J. M. Electron and Hole Transport in Poly(P-phenylene Vinylene) Devices. *Appl. Phys. Lett.* **1996**, *68*, 3308–3310.
- (9) Kepler, R. G. Charge Carrier Production and Mobility in Anthracene Crystals. *Phys. Rev.* **1960**, *119*, 1226–1229.
- (10) Liu, F.; Massé, A.; Friederich, P.; Symalla, F.; Nitsche, R.; Wenzel, W.; Coehoorn, R.; Bobbert, P. A. Ab Initio Modeling of Steady-State and Time-Dependent Charge Transport in Hole-Only α -NPD Devices. *Appl. Phys. Lett.* **2016**, *109*, 243301.
- (11) Friederich, P.; Fediai, A.; Kaiser, S.; Konrad, M.; Jung, N.; Wenzel, W. Toward Design of Novel Materials for Organic Electronics. *Adv. Mater.* **2019**, *31*, 1808256.
- (12) Symalla, F.; Friederich, P.; Massé, A.; Meded, V.; Coehoorn, R.; Bobbert, P.; Wenzel, W. Charge Transport by Superexchange in Molecular Host-Guest Systems. *Phys. Rev. Lett.* **2016**, *117*, 276803.
- (13) Symalla, F.; Friederich, P.; Kaiser, S.; Strunk, T.; Neumann, T.; Wenzel, W. 26-4: Computer-Aided Optimization of Multilayer OLED Devices. *SID Symp. Dig. Tech. Pap.* **2018**, *49*, 340–342.
- (14) Symalla, F.; Heidrich, S.; Kubillus, M.; Strunk, T.; Neumann, T.; Wenzel, W. 19-4: Boosting OLED Performance with Ab-Initio Modeling of Roll-off and Quenching Processes. *SID Symp. Dig. Tech. Pap.* **2019**, *50*, 259–262.
- (15) Symalla, F.; Fediai, A.; Armleder, J.; Kaiser, S.; Strunk, T.; Neumann, T.; Wenzel, W. 43-3: Ab-Initio Simulation of Doped Injection Layers. *SID Symp. Dig. Tech. Pap.* **2020**, *51*, 630–633.

- (16) Symalla, F.; Heidrich, S.; Friederich, P.; Strunk, T.; Neumann, T.; Minami, D.; Jeong, D.; Wenzel, W. Multiscale Simulation of Photoluminescence Quenching in Phosphorescent OLED Materials. *Adv. Theory Simul.* **2020**, *3*, 1900222.
- (17) Kotadiya, N. B.; Mondal, A.; Xiong, S.; Blom, P. W. M.; Andrienko, D.; Wetze-laer, G.-J. A. H. Rigorous Characterization and Predictive Modeling of Hole Transport in Amorphous Organic Semiconductors. *Adv. Electron. Mater.* **2018**, *4*, 1800366.
- (18) van der Holst, J. J. M.; van Oost, F. W. A.; Coehoorn, R.; Bobbert, P. A. Monte Carlo Study of Charge Transport in Organic Sandwich-Type Single-Carrier Devices: Effects of Coulomb Interactions. *Phys. Rev. B* **2011**, *83*, 085206.
- (19) Liu, F.; van Eersel, H.; Xu, B.; Wilbers, J. G. E.; de Jong, M. P.; van der Wiel, W. G.; Bobbert, P. A.; Coehoorn, R. Effect of Coulomb Correlation on Charge Transport in Disordered Organic Semiconductors. *Phys. Rev. B* **2017**, *96*, 205203.
- (20) Neumann, T.; Danilov, D.; Lennartz, C.; Wenzel, W. Modeling Disordered Morphologies in Organic Semiconductors. *J. Comput. Chem.* **2013**, *34*, 2716–2725.
- (21) Friederich, P.; Symalla, F.; Meded, V.; Neumann, T.; Wenzel, W. Ab Initio Treatment of Disorder Effects in Amorphous Organic Materials: Toward Parameter Free Materials Simulation. *J. Chem. Theory Comput.* **2014**, *10*, 3720–3725.
- (22) Baumeier, B.; Stenzel, O.; Poelking, C.; Andrienko, D.; Schmidt, V. Stochastic Modeling of Molecular Charge Transport Networks. *Phys. Rev. B* **2012**, *86*, 184202.
- (23) Kohn, W.; Sham, L. J. Self-Consistent Equations Including Exchange and Correlation Effects. *Phys. Rev.* **1965**, *140*, A1133–A1138.
- (24) Ahlrichs, R.; Bär, M.; Häser, M.; Horn, H.; Kölmel, C. Electronic Structure Calculations on Workstation Computers: The Program System Turbomole. *Chem. Phys. Lett.* **1989**, *162*, 165–169.
- (25) Stephens, P. J.; Devlin, F. J.; Chabalowski, C. F.; Frisch, M. J. Ab Initio Calculation of Vibrational Absorption and Circular Dichroism Spectra Using Density Functional Force Fields. *J. Phys. Chem.* **1994**, *98*, 11623–11627.
- (26) Weigend, F.; Ahlrichs, R. Balanced Basis Sets of Split Valence, Triple Zeta Valence and Quadruple Zeta Valence Quality for H to Rn: Design and Assessment of Accuracy. *Phys. Chem. Chem. Phys.* **2005**, *7*, 3297–3305.
- (27) Friederich, P.; Rodin, V.; von Wrochem, F.; Wenzel, W. Built-In Potentials Induced by Molecular Order in Amorphous Organic Thin Films. *ACS Appl. Mater. Interfaces* **2018**, *10*, 1881–1887.
- (28) Hastings, W. K. Monte Carlo Sampling Methods Using Markov Chains and Their Applications. *Biometrika* **1970**, *57*, 97–109.
- (29) Nelsen, S. F.; Blackstock, S. C.; Kim, Y. Estimation of Inner Shell Marcus Terms for Amino Nitrogen Compounds by Molecular Orbital Calculations. *J. Am. Chem. Soc.* **1987**, *109*, 677–682.
- (30) Löwdin, P.-O. On the Non-Orthogonality Problem Connected with the Use of Atomic Wave Functions in the Theory of Molecules and Crystals. *J. Chem. Phys.* **1950**, *18*, 365–375.
- (31) Stehr, V.; Pfister, J.; Fink, R. F.; Engels, B.; Deibel, C. First-Principles Calculations of Anisotropic Charge-Carrier Mobilities in Organic Semiconductor Crystals. *Phys. Rev. B* **2011**, *83*, 155208.
- (32) Becke, A. D. Density-Functional Exchange-Energy Approximation with Correct Asymptotic Behavior. *Phys. Rev. A* **1988**, *38*, 3098–3100.

- (33) Perdew, J. P. Density-Functional Approximation for the Correlation Energy of the Inhomogeneous Electron Gas. *Phys. Rev. B* **1986**, *33*, 8822–8824.
- (34) Friederich, P.; Meded, V.; Poschlad, A.; Neumann, T.; Rodin, V.; Stehr, V.; Symalla, F.; Danilov, D.; Lüdemann, G.; Fink, R. F.; Kondov, I.; von Wrochem, F.; Wenzel, W. Molecular Origin of the Charge Carrier Mobility in Small Molecule Organic Semiconductors. *Adv. Funct. Mater.* **2016**, *26*, 5757–5763.
- (35) Massé, A.; Coehoorn, R.; Bobbert, P. A. Universal Size-Dependent Conductance Fluctuations in Disordered Organic Semiconductors. *Phys. Rev. Lett.* **2014**, *113*, 116604.
- (36) Marcus, R. A. On the Theory of Oxidation-Reduction Reactions Involving Electron Transfer. I. *J. Chem. Phys.* **1956**, *24*, 966–978.
- (37) Ewald, P. P. Die Berechnung Optischer Und Elektrostatischer Gitterpotentiale. *Ann. Phys.* **1921**, *369*, 253–287.
- (38) Miller, A.; Abrahams, E. Impurity Conduction at Low Concentrations. *Phys. Rev.* **1960**, *120*, 745–755.
- (39) Kröger, M.; Hamwi, S.; Meyer, J.; Riedl, T.; Kowalsky, W.; Kahn, A. P-Type Doping of Organic Wide Band Gap Materials by Transition Metal Oxides: A Case-Study on Molybdenum Trioxide. *Org. Electron.* **2009**, *10*, 932–938.
- (40) White, R. T.; Thibau, E. S.; Lu, Z.-H. Interface Structure of MoO₃ on Organic Semiconductors. *Sci. Rep.* **2016**, *6*, 21109.
- (41) Kahn, A.; Koch, N.; Gao, W. Electronic Structure and Electrical Properties of Interfaces between Metals and π -Conjugated Molecular Films. *J. Polym. Sci., Part B: Polym. Phys.* **2003**, *41*, 2529–2548.
- (42) Chu, T.-Y.; Song, O.-K. Apparent Thickness Dependence of Mobility in Organic Thin Films Analyzed by Gaussian Disorder Model. *J. Appl. Phys.* **2008**, *104*, 023711.
- (43) van Mensfoort, S. L. M.; Shabro, V.; de Vries, R. J.; Janssen, R. a. J.; Coehoorn, R. Hole Transport in the Organic Small Molecule Material α -NPD: Evidence for the Presence of Correlated Disorder. *J. Appl. Phys.* **2010**, *107*, 113710.
- (44) Anthopoulos, T. D.; Markham, J. P. J.; Nandas, E. B.; Samuel, I. D. W.; Lo, S.-C.; Burn, P. L. Highly Efficient Single-Layer Dendrimer Light-Emitting Diodes with Balanced Charge Transport. *Appl. Phys. Lett.* **2003**, *82*, 4824–4826.